CHEMISTRY OF MATERIALS

pubs.acs.org/cm

Article

Design of Low Crystallinity Spiro-Typed Hole Transporting Material for Planar Perovskite Solar Cells to Achieve 21.76% Efficiency

Zihao Deng, Maosheng He, Yi Zhang, Fateh Ullah, Kui Ding, Jianghu Liang, Zhanfei Zhang, Heng Xu, Yuankun Qiu, Ziyi Xie, Tong Shan, Zhenhua Chen, Hongliang Zhong, and Chun-Chao Chen*

Cite This: https://dx.doi.org/10.1021/acs.chemmater.0c03772

Read Online

ACCESS | Metrics & More | Article Recommendations | Supporting Information

ABSTRACT: Hole transporting materials (HTMs) play a crucial role in achieving highly efficient and stable perovskite solar cells (PSCs). Spiro-typed materials being the most widely used HTMs are commonly utilized with dopants, such as Li-TFSI, to improve their carrier mobility significantly. However, dopants could affect the morphology of hole transporting layer negatively by forming defects and pinholes which restrict the performance of devices. Here, we adopt the extended π-conjugated structures *N*-ethylcarbazole and dibenzothiophene to substitute the donor group 4-methoxyphenyl of spiro-OMeTAD, devising two novel HTMs, SC and ST, respectively. Notably, SC possesses low crystallinity and good solubility due to the existence of ethyl in side groups, leading to decent miscibility with Li-TFSI to prevent unfavorable phase-separation. The SC-based device delivers the best power conversion efficiency (PCE) of 21.76% which is higher than that of spiro-OMeTAD (20.73%), attributed to the formation of smooth and pinhole-free morphology. Moreover, it exhibits long-term stability and retains over 90% of initial PCE value for more than 30 days without encapsulation in ambient air. In contrast, the ST-based device suffers from dense pinholes induced by its relatively high crystallinity and poor solubility, resulting in a low PCE of 18.18% and inferior stability. Thus, it is effective to modify the side groups in spiro-typed HTMs with specific structures to obtain predictable properties, fabricating PSCs with high efficiency and stability facilely.

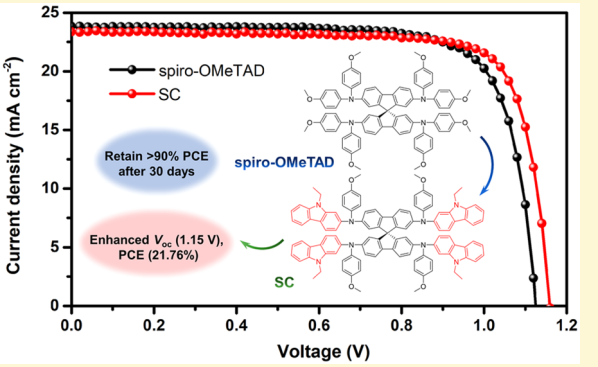

INTRODUCTION

Over the past decade, organic−inorganic hybrid perovskite solar cells (PSCs) have attracted considerable attention due to their low cost,[1] facile fabrication,[2] and particularly excellent power conversion efficiencies (PCEs), which increased from 3.8% to 25.2%.[3−8] Because of prominent light absorption, tunable bandgaps, high charge carrier mobility, and long exciton lifetime, PSCs develop so rapidly that they are comparable with polycrystalline silicon solar cells.[9−16] In addition to active layers, the efficiency and stability of cells are strongly dependent on the device structure and the properties of the charge transporting interfacial materials being used.[17−22] In general, hole transporting materials (HTMs) are responsible to extract holes from perovskite to electrodes. They play an important role in reducing nonradiative recombination and achieving high efficiencies of the devices.[23−29] Meanwhile, it also contributes to the lifetime of perovskite solar cells.[30−33]

Nowadays, 2,2′,7,7′-tetrakis(*N*,*N*-di-*p*-methoxyphenylamino)-9,9′-spirobifluorene, also known as spiro-OMeTAD, which was first utilized by Park's group in PSCs,[4] is the most widely used HTM in this region. However, it suffers from low conductivity and hole mobility,[34] therefore, dopants such as 4-*tert*-butylpyridine (*t*-BP), lithium bis-(trifluoromethanesulfonyl)imide (Li-TFSI) are added into spiro-OMeTAD to enhance its ability to transfer hole carriers.[35] These dopants are, however, detrimental to perovskite solar cell's stability by accelerating the speed of humidity diffusion into perovskite and causing the degradation irreversibly.[36−38] Therefore, researchers devised various D-A-D or D-π-D typed HTMs with different cores to realize dense molecular $\pi-\pi$ stacking and impressive hole mobility, attempting to remove dopants to reinforce the long-term stability of PSCs.[39,40] With the introduction of diverse functional groups and heteroatoms (like sulfur, nitrogen), HTMs could modify the coarse surface of perovskite or passivate defects as well.[41,42] Although these eminent works put forward efficient strategies to design novel HTMs without dopants, only a few of them could exhibit better performance than spiro-OMeTAD, such as DTP-C6Th.[43] More impor-

Received: September 23, 2020
Revised: December 12, 2020

Scheme 1. Process of Film Forming Based on spiro-OMeTAD, SC, and ST with Dopants

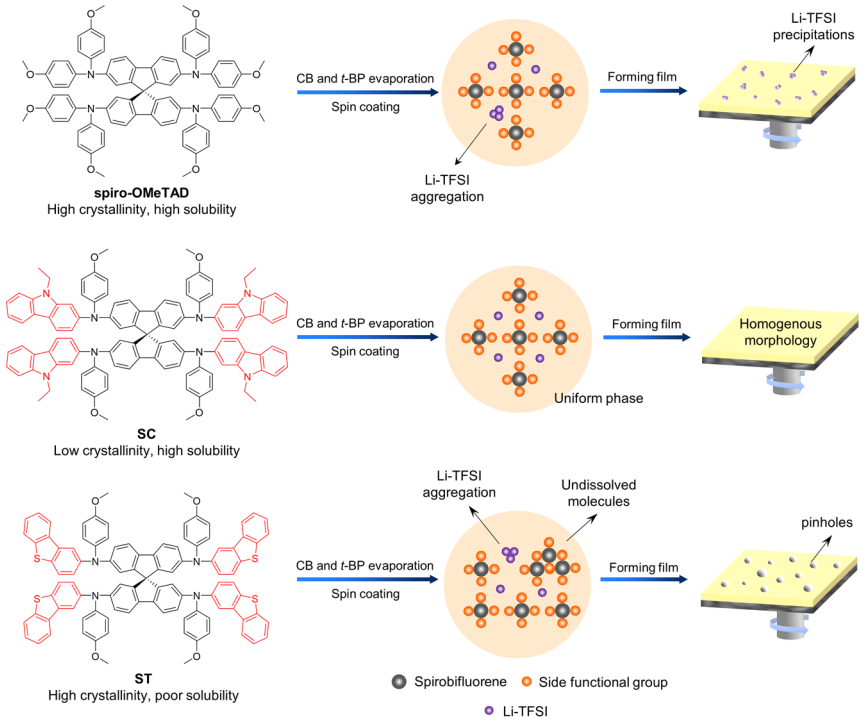

tantly, most of highly efficient doping-free HTMs are only used for *p-i-n* typed PSCs, confining its application significantly.[40,44−46] Hence, it is still imperative to research HTMs with dopants and improve the stability of PSCs, while maintaining high efficiencies of the devices.

As for spiro-typed HTMs, devices fabricated with them can exhibit excellent efficiencies. In the early stage, researchers modified the spirobifluorene core to enhance the performance of spiro-OMeTAD.[47] With facile synthesis, Sun et al. used spiro[fluorene-9,9′-xanthene] (SFX) core to fabricate novel HTMs X59 and X60 with PCEs of 19.8% and 19.84%, respectively, showing better performance than that of spiro-OMeTAD.[48,49] Also, its derivative X55 also achieved a promising PCE of 20.8% with long-term stability.[50] Besides, Nazeeruddin et al. reported a dissymmetric fluorene-dithiophene core (FDT) whose sulfur atoms could coordinate with Pb^{2+} in perovskite effectively, promoting the ability of HTM to extract holes.[51] The device based on FDT delivered an impressive PCE of 20.2%. Gradually, spiro-typed HTMs being the most widely used HTMs determine the efficiency and stability outcome of PSCs. Nevertheless, the modification of side groups to provide spiro-typed HTMs with various properties is often neglected. Sparsely, Sang Il Seok et al. discussed the property variations of spiro-OMeTAD caused by the different positions of methoxy substituents systematically.[52] Wei Huang et al. analyzed the effects of heteroatom substitution of methoxy groups.[53]

To further push toward efficiency limits, Jangwon Seo et al. reported a fluorene-terminated spiro-typed HTM DM with a fine-tuned energy level, enhancing V_{oc} of devices and obtaining the best PCE value of 23.2% with good stability.[54] However, the effects of side functional groups on the photovoltaic properties of spiro-typed HTMs have not been fully explored yet. Moreover, the effect of crystallinity and solubility of molecules on their morphology is neglected. Although the strong tendency of crystallization and enhanced $\pi-\pi$ stacking could help HTMs to extract carriers efficiently, dopants are prone to aggregate around the grain boundary, leading to the precipitation of Li-salts or the formation of pinholes in the film.[38,55] Hence, it is important to find an optimized condition for both morphology and efficient carriers transporting capacity by devising novel molecules as HTMs with the fine-tuned properties to realize the reliable performance of devices.

In this work, we designed two novel spiro-typed HTMs by the substitution of side groups with *N*-ethylcarbazole and dibenzothiophene, which are used for photovoltaic devices widely due to their excellent electrical properties, obtaining *N*,$^2N^{2\prime}$,N^7,$N^{7\prime}$-tetrakis(9-ethyl-9*H*-carbazol-2-yl)-N^2,$N^{2\prime}$,N^7,$N^{7\prime}$-tetrakis(4-methoxyphenyl)-9,9′-spirobi[fluorene]-2,2′,7,7′-tetraamine (SC) and N^2,$N^{2\prime}$,N^7,$N^{7\prime}$-tetrakis(dibenzo[*b*,*d*]thiophen-2-yl)-N^2,$N^{2\prime}$,N^7,$N^{7\prime}$-tetrakis(4-methoxyphenyl)-9,9′-spirobi[fluorene]-2,2′,7,7′-tetraamine (ST) respectively, as shown in Scheme 1. With the introduction of extended π-conjugated structures with weak electron-donating ability, we aim to lower the highest occupied molecular orbital (HOMO) level of spiro-typed HTMs, assisting the formation of larger V_{oc} to promote the performance of devices. Notably, the alkyl chains in *N*-ethylcarbazole increase the solubility and reduce the crystallinity of SC, leading to favorable miscibility with dopants and uniform morphology of the film. Based on triple-cation mixed perovskite $(CsPbI_3)_x(FAPbI_3)_y(MAPbBr_3)_{1-x-y}$ in the planar structure, the device with SC obtains the best PCE value of 21.76%, ascribed to the enhancement of V_{oc} (1.15 V) and FF (80.62%) benefitted from the deep HOMO level and good film forming ability of SC, giving better performance than that of spiro-OMeTAD (20.73%). Meanwhile, due to the increase of molecular weight and hydrophobicity, the device can retain over 90% of the original PCE for more than 30 days in ambient air (25 °C; relative humidity, 30 ± 5%) without encapsulation, performing excellent humid and thermal durability as well. In contrast, although ST has similar physical properties to SC,

https://dx.doi.org/10.1021/acs.chemmater.0c03772
Chem. Mater. XXXX, XXX, XXX−XXX

Table 1. Optical, Electrochemical, Thermal, and Electrical Properties of spiro-OMeTAD, SC, and ST

HTM	$\lambda_{max}/\lambda_{edge}$ [a] (nm)	E_g [b] (eV)	E_{HOMO} (eV)	E_{LUMO} (eV)	T_d (°C)	T_g (°C)	T_m (°C)	mobility ($cm^2\ V^{-1}\ s^{-1}$)
spiro-OMeTAD	313, 377/413	3.00	−5.22[c]/−4.23[d]	−2.22[c]/−0.65[d]	438.3	122.0	247.9	5.88×10^{-3}
SC	351, 395/426	2.91	−5.26[c]/−4.32[d]	−2.35[c]/−0.86[d]	459.4	163.7	275.5	3.15×10^{-3}
ST	315, 379/418	2.97	−5.31[c]/−4.40[d]	−2.34[c]/−1.00[d]	458.5	159.9	273.2	1.77×10^{-3}

[a]Measured in the solid state. [b]Calculated from UV−vis absorption spectra. [c]HOMO and LUMO energy levels estimated from the redox potential in cyclic voltammetry and UV−vis absorption spectra. [d]Calculations of DFT.

due to its high crystallinity and poor miscibility with dopants, the ST-based device suffers from pinholes in the film so that it displays inferior efficiency (18.18%) and stability. Conclusively, we demonstrate that the utilization of extended π-conjugated functional groups to endow spiro-typed HTMs with improved solubility and reduced crystallinity is a reliable strategy to promote the distribution of Li-TSFI in the solid film so that highly efficient and stable devices can be constructed.

RESULTS AND DISCUSSION

Although PSCs exhibit excellent performance, many devices still suffer from nonradiative recombination and V_{oc} loss which are induced by the formation of pinholes and the precipitation of dopants at the hole transporting layer fabricated by spiro-OMeTAD.[38] To eliminate such negative effects, it is valuable to investigate the physical properties of various spiro-typed HTMs to improve the morphology of interfaces. Besides simple π-conjugated structures, *N*-ethylcarbazole and dibenzothiophene also show extraordinary electrical properties and promising prospects in photovoltaic regions as basic building blocks.[56,57] Here, we aim to introduce these two similar building blocks to substitute 4-methoxyphenyl of spiro-OMeTAD. Due to different functional groups in these moieties, it is effective to explore the effects of prolonged conjugated structures on HTMs, the alterations of morphology caused by the variations of solubility and crystallinity of molecules, and the ability of carrier transport at the interface. So, we can conclude a reasonable way to modify spiro-typed HTMs to construct PSCs with high efficiency and stability.

The synthetic routes of SC and ST are shown in Schemes S1 and S2, and detailed procedures are depicted in the Experimental Section. Briefly, *N*-ethylcarbazole was prepared according to the previous reports.[58] Then the intermediates 1 and 2 were synthesized via Buchwald−Hartwig coupling. Finally, the target compounds were also prepared by Buchwald−Hartwig coupling readily, giving SC and ST with yields of 52% and 50%, respectively. Meanwhile, the two materials are readily soluble in chlorobenzene (CB) and chloroform. The synthesis cost of three HTMs is calculated in Tables S5−S7, giving the consumption of spiro-OMeTAD, SC, and ST could be 22.29 ¥, 21.60 ¥, and 20.19 ¥, respectively, for each experiment. These molecular structures were characterized by ^{1}H NMR spectroscopy, ^{13}C NMR spectroscopy, and matrix-assisted laser desorption-ionization-time-of-flight (MALDI-TOF) mass spectrometry (Figures S1−S10).

The physical properties of HTMs are summarized in Table 1. The UV−vis spectra of HTMs in the film state are shown in Figure 1a. Compared to spiro-OMeTAD, a slight bathochromic shift is noted that the maximum absorption peaks of SC and ST are presented at 395 and 379 nm, respectively, while the peak of spiro-OMeTAD appears at 377 nm, representing the π−π* transition. The red-shift of peaks is attributed to the extension of the π-conjugated structure.[59]

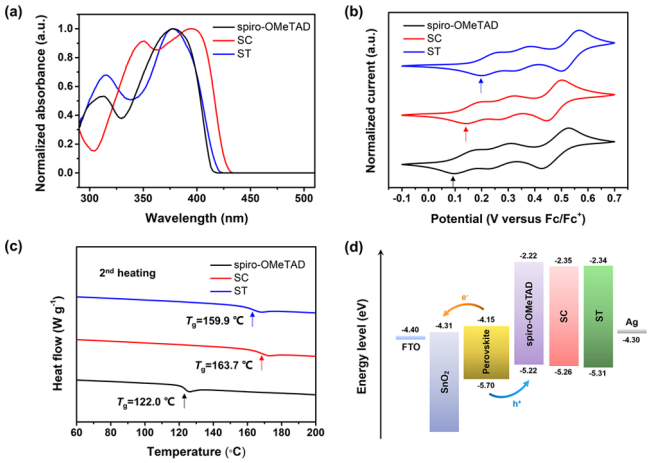

Figure 1. (a) Normalized UV−vis absorption spectra of spiro-OMeTAD, SC, and ST in the solid state. (b) Cyclic voltammograms of spiro-OMeTAD, SC, and ST in CH_2Cl_2 solution; the arrows indicate the first peak cathodic potentials. (c) DSC curves of spiro-OMeTAD, SC, and ST; the arrows indicate the glass transition temperature. (d) The energy level diagram of the components in the device.

Notably, such a phenomenon is less evident for ST, which is interpreted by the strong electron-withdrawing ability of dibenzothiophene. Moreover, the change of molecular configuration could also enhance their absorption in the region of 300−400 nm, exhibiting larger absorption intensity than that of spiro-OMeTAD. According to the absorption edges of spectra, the optical bandgap (E_g) of spiro-OMeTAD, SC, and ST can be calculated as 3.00, 2.91, and 2.97 eV, respectively. Moreover, the band gap value of perovskite is also obtained from Figure S12a as 1.55 eV. All of the HTMs do not affect the optical property of perovskite because of their weak absorption in the visible light region.

Cyclic voltammetry (CV) was used to estimate energy levels of HTMs by dissolving them into dichloromethane with tetrabutylammonium hexafluorophosphate (0.1 M). The oxidation and reduction curves are displayed in Figure 1b. Regarding the HOMO level of spiro-OMeTAD as −5.22 eV,[54] the HOMO levels of SC and ST are calculated as −5.26 eV and −5.31 eV, respectively. The HOMO levels of HTMs are coordinated with that of perovskite (−5.70 eV) to extract holes. With the bandgap results from UV−vis spectra, the lowest unoccupied molecular orbital (LUMO) levels of SC and ST are determined as −2.35 eV and −2.34 eV, respectively, as shown in Table 1. Furthermore, ultraviolet photoelectron spectroscopy (UPS) was used to confirm the HOMO levels of HTMs in the solid state. The cutoff (E_{cutoff}) and onset (E_{onset}) energy regions in the spectra are depicted in Figure S11b−d. The HOMO levels of spiro-OMeTAD, SC, and ST are calculated as −5.05 eV, −5.09 eV, and −5.17 eV, respectively, which are consistent with the tendency measured from CV

https://dx.doi.org/10.1021/acs.chemmater.0c03772
Chem. Mater. XXXX, XXX, XXX−XXX

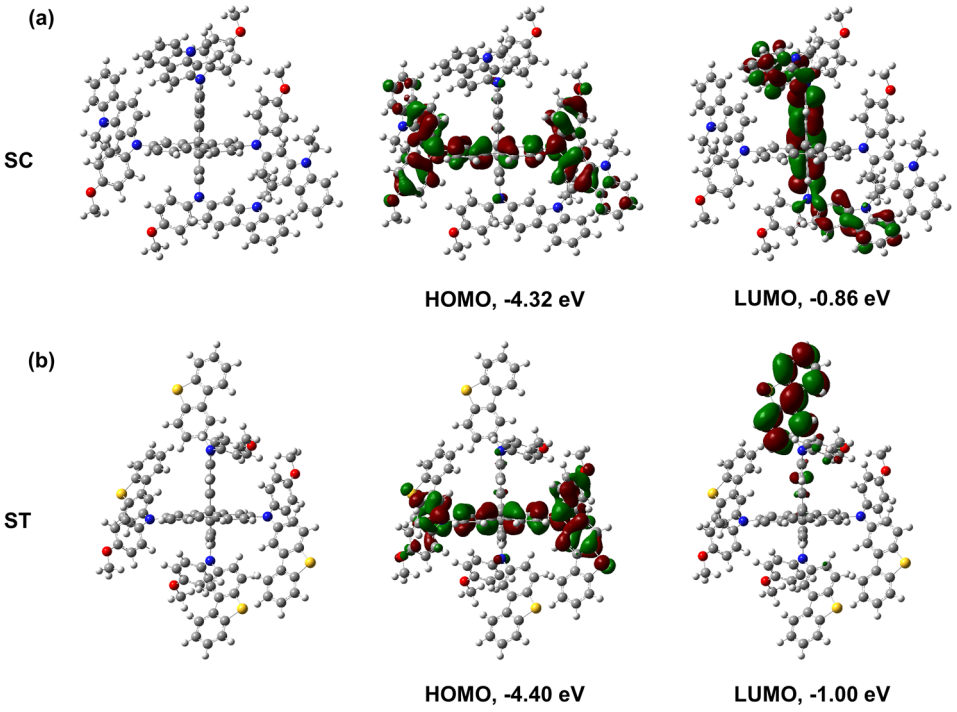

Figure 2. Optimized molecular structures and DFT calculations of HOMO and LUMO levels of (a) SC and (b) ST.

curves. Similarly, the HOMO and LUMO levels of perovskite could be estimated to be −5.70 eV and −4.15 eV, respectively, based on the spectra of UPS (Figure S11a) and optical bandgap values. More importantly, the barriers of LUMO levels between perovskite and HTMs are large enough to block the motion of electrons and suppress the radiative recombination.[60] The energy level diagram of the components in the device is depicted in Figure 1d.

Meanwhile, density functional theory (DFT) calculations were performed to simulate spatial structures and distribution of electrons at the B3LYP/6-31G (d) level,[60] and the results are concluded in Figure 2 and Table 1. Similarly, the two planar fluorenes are almost perpendicular to each other at the fixed spiro carbon, forming the cores of these HTMs. As for SC, due to the diverse dihedral angles between side groups and the core, which leads to different intramolecular interactions, the HOMO and LUMO are located at one of the planar fluorenes independently. Such a distribution is similar to that of spiro-OMeTAD (Figure S13). However, SC shows more extended delocalization of HOMO and LUMO over carbazole moieties due to the prolonged π-conjugation. Notably, the *N*-ethylcarbazole of SC is a weaker donor than the 4-methoxyphenyl of spiro-OMeTAD. It is ascribed to the fact that the π-donor N atom of carbazole is meta (cross-conjugated) from the tertiary amine attached to the spirobifluorene, whereas the methoxyl of spiro-OMeTAD is para conjugated. Hence its HOMO level is reduced from −4.23 eV to −4.32 eV reasonably. On the other hand, the HOMO of ST also exhibits widely extended distribution as SC. Nevertheless, its LUMO is mainly localized on a specific dibenzothiophene moiety because of the electron-withdrawing property of side groups, showing centralized distribution and weak conjugation effect with the core so that the charge transfer is restricted. As a result, it causes the decreases of HOMO and LUMO levels to −4.40 eV and −1.00 eV, respectively, corresponding to the tendency of CV curves. Inversely, if we use functional groups with strong electron-donating abilities and reduced conjugative structures, the HOMO level could be elevated. Thus, the energy levels of spiro-typed HTMs can be fine-tuned.[53,54]

The thermal properties of HTMs were characterized by thermogravimetric analysis (TGA) and differential scanning calorimetry (DSC) measurements. As shown in Figure S12b, with the increase of molecular weight, stronger intermolecular forces endow SC and ST with higher decomposition temperatures (T_d) of 459.4 and 458.5 °C, respectively, as compared to 438.3 °C of spiro-OMeTAD, exhibiting considerable thermal stability. Moreover, DSC curves in Figure 1c show high glass transition temperatures (T_g) of them, reaching 163.7 and 159.9 °C, respectively, which are about 40 °C higher than that of spiro-OMeTAD. These results demonstrate the strong tendency of SC and ST to resist the change of molecular arrangement in working conditions, showing good potential to sustain thermal stability in devices with dopants. Meanwhile, in Figure S12c, the melting peaks in DSC also reflect their ability to crystallize. Both spiro-OMeTAD and ST exhibit large melting enthalpy at 247.9 and 273.2 °C, respectively, demonstrating their strong tendency of crystallization relatively. SC gives a much lower endothermic peak at 275.5 °C, which indicates its lower relative crystallinity.[51,61]

The neat interface morphology of HTMs is dominant for devices to achieve desirable performance. 2D grazing incidence wide-angle X-ray scattering (2D-GIWAXS) was employed to investigate relative crystallinity and molecular orientation of them. As depicted in Figure 3, all spiro-typed HTMs give uniform distributions of diffraction intensity, indicating the existence of crystallites without any preferential orientation in films. From 1D GIWAXS analysis along the out-of-plane direction in Figure S14a, spiro-OMeTAD shows a strong $\pi-\pi$ stacking diffraction peak by the (010) orientation at ∼14.25 nm^{-1}, with an interplanar separation of $D = 2\pi/q_z$ = 4.41 Å.

https://dx.doi.org/10.1021/acs.chemmater.0c03772
Chem. Mater. XXXX, XXX, XXX−XXX

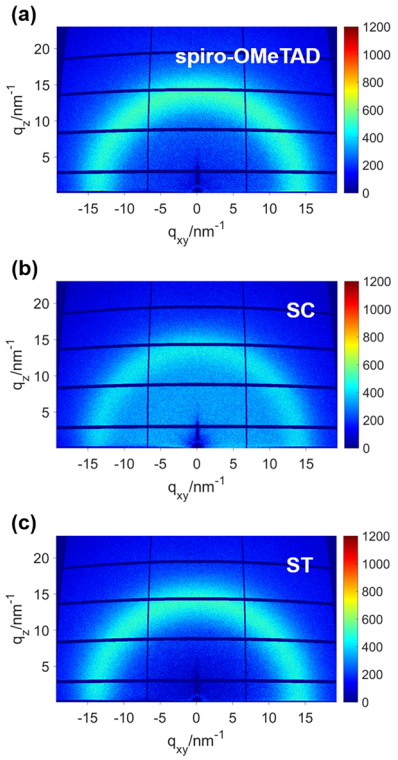

Figure 3. 2D GIWAXS patterns of (a) spiro-OMeTAD, (b) SC, and (c) ST.

Although ST has a more rigid conjugated structure for reinforcing stacking, it does not exhibit much stronger intensity than spiro-OMeTAD due to the steric effect of larger side groups, giving a comparable $\pi-\pi$ stacking (010) diffraction intensity at a similar position (~14.30 nm^{-1}) along the out-of-plane direction, with a packing distance of 4.39 Å. It suggests that both of them possess a considerable amount of ordered crystallites to achieve high crystallinity which could promote hole transportation in PSCs. In contrast, the steric effect of rigid side moieties and vibrational motions of ethyl groups in SC disturb the ordered molecular arrangement in film significantly. The $\pi-\pi$ stacking (010) peak with the weakest intensity at 13.96 nm^{-1} along the out-of-plane direction is found for SC, confirming its relatively lower crystallinity and charge transfer ability.[62−64] In Table S1, $\pi-\pi$ stacking distance D of HTMs are summarized. SC, with the largest D among HTMs (D = 4.50 Å), possesses the weakest intermolecular interaction which inhibits the formation of many ordered crystallites, reflecting its poorest ability of crystallization as well.[65,66] Without preferential orientation, in-plane direction analysis, as shown in Figure S14b, shares similar results with the out-of-plane analysis above. Furthermore, since the crystallization of molecules can enhance the surface roughness, the AFM images of the pristine films of HTMs are also provided in Figure S15. SC with the smoothest morphology among HTMs (RMS roughness = 3.94 nm) shows the least tendency to form crystallized regions.

Moreover, in order to evaluate the morphology of HTMs used in devices under the optimal condition, top-view scanning electron microscopy (SEM) images of pristine perovskite $(CsPbI_3)_x(FAPbI_3)_y(MAPbBr_3)_{1-x-y}$ that is coated with different HTMs are presented in Figure 4a−d. Figure 4a shows the uniform perovskite film fabricated by a two-step method with high quality, promoting the generation and transfer of carriers efficiently. When the HTMs, spiro-OMeTAD and SC, are deposited onto the surface of perovskite, the contrast of images declines drastically, indicating the formation of smooth films to extract holes. However, compared with the homogeneous morphology of SC, the film of spiro-OMeTAD exists as small bright spots attributed to the precipitation of dopants (Li-TFSI) on the surface, which could cause negative effects on the efficiency and stability of devices. As a comparison, the perovskite coated by ST has many pinholes in the surface, restraining the transfer of holes because of the reduced effective contact area between the active layer and electrodes, resulting in severe nonradiative recombination of carriers around defects.[67,68] To detect the microstructures more precisely and intuitively, the roughness of films was measured by atomic force microscopy (AFM). As shown in Figure 4e−h, the root-mean-square (RMS) roughness of perovskite (36.5 nm) decreases sharply after covering with HTMs. As for SC, the RMS roughness of film is reduced to 5.24 nm, exhibiting good film forming ability with dopants. Meanwhile, large RMS

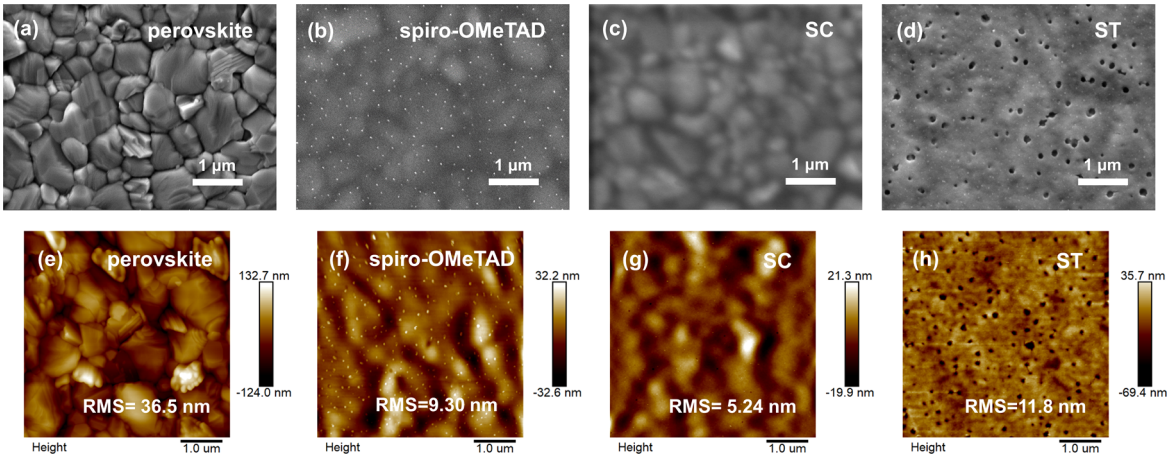

Figure 4. Top-view SEM images of (a) pristine perovskite film, (b) perovskite covered with spiro-OMeTAD, (c) perovskite covered with SC, and (d) perovskite covered with ST doped with 54 μL of Li-TFSI solution, respectively. AFM images of (e) pristine perovskite film, (f) perovskite covered with spiro-OMeTAD, (g) perovskite covered with SC, and (h) perovskite covered with ST doped with 54 μL of Li-TFSI solution, respectively.

https://dx.doi.org/10.1021/acs.chemmater.0c03772
Chem. Mater. XXXX, XXX, XXX−XXX

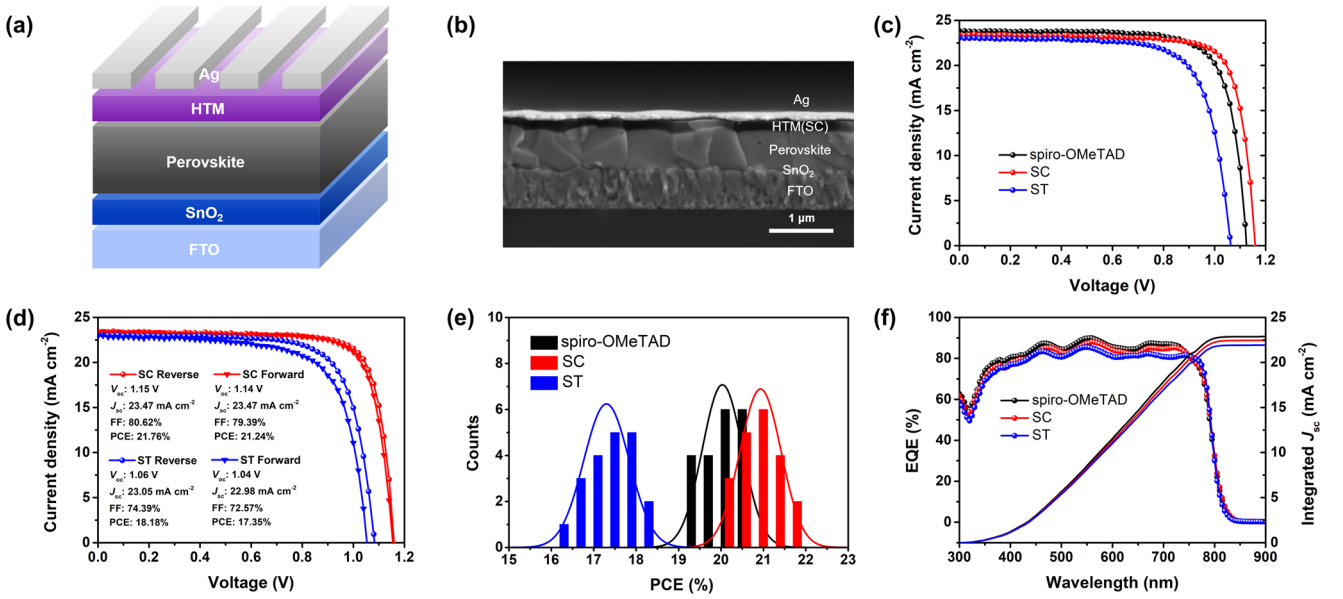

Figure 5. (a) Device structure of PSCs (FTO/SnO_2/perovskite/HTM/Ag). (b) Cross-sectional SEM image of device with SC as HTM. (c) $J-V$ curves of the best performing devices based on three HTMs under reverse scanning. (d) Reverse and forward scanning $J-V$ curves of optimal devices based on SC and ST, respectively. (e) PCE distribution histogram of 20 devices with three HTMs. (f) EQE spectra and integrated current density of PSCs based on spiro-OMeTAD, SC, and ST.

roughness values of 9.30 and 11.8 nm are found for spiro-OMeTAD and ST-based devices, respectively, showing an undesirable surface morphology.

Furthermore, the morphology of HTMs with high concentrations of dopants was also investigated to analyze the effect of Li-salts comprehensively. As shown in Figure S16, with the addition of Li-TFSI solution (170 mg/mL in acetonitrile) increased from the optimal concentration (54 μL) to a high concentration of 80 μL in 1 mL of HTM solution, the film made by SC maintains a similar RMS roughness as before (6.56 nm), exhibiting a considerable tolerance for the dopant concentration. In contrast, the high dopants concentration makes the coating of spiro-OMeTAD much less uniform than before, accompanied by the denser distribution of Li-TFSI precipitations and coarser surface with RMS roughness of 11.0 nm. In the case of ST, the high concentration of Li-TFSI raises severe damage to the film of ST by increasing the size and depth (from ~70 to 200 nm) of pinholes greatly, performing large RMS roughness (38.4 nm), so that it is no longer capable of being used as HTM to transport holes. In conclusion, SC possesses the best film forming ability with a large processing window of dopant concentrations.

The time-of-flight-secondary ion mass spectrometry (TOF-SIMS) was used to analyze the distribution of Li-salts in the film of HTMs qualitatively. Here, the optimized lithium dopant concentration (54 μL) was used for HTMs. Upon the different sputtering time, the distribution of dopants can be reflected from the signal profile of the fluorine atom, which is a representative constituent of Li-TFSI. As shown in Figure S17d, from the sputtering time 0 to 10 s, dopant distributions near the surface are obtained. Here, a significantly large content of fluorine is detected in spiro-OMeTAD and ST. This can be ascribed to the precipitations of dopants on the surface. From the sputtering time 10 to 70 s, the films of spiro-OMeTAD and ST exhibit less content of dopants as compared to that of SC, indicating the reduction of dopants in the bulk. Oppositely, the fluorine content of SC shows no increase in the early stage and is uniformly distributed inside the film. In Figure S17a–c, the TOF-SIMS mappings in the sputtering time 0 to 70 s of fluorine atoms in bulk are shown. Slight aggregation of fluorine in ST can be seen. When the concentration of Li-TFSI is increased to 80 μL, the ST-based film shows severe segregation of Li-salts around the pinholes, as shown in Figure S18c. Both spiro-OMeTAD and SC still possess a uniform distribution of dopants.

Meanwhile, UV–vis spectroscopy was also utilized to analyze the formation and distribution of radical cations (like spiro-OMeTAD$^{\bullet+}$) of HTMs in the solid state. It is reasonable to conclude that the uniform distribution of dopants facilitates the oxidation of molecules homogeneously, leading to the enhancement of the specific absorption peak.[69,70] Figure S19a,b shows the absorption of HTMs films doped by the optimal concentration of dopants under the AM 1.5G illumination for 1 h in ambient conditions. The film of SC gives the highest intensity of absorption around 535 nm, attributed to the uniform generation of oxidized SC$^{\bullet+}$. In the case of spiro-OMeTAD, it exhibits a lower absorption peak around 530 nm, demonstrating its slightly inferior miscibility with dopants as compared to that of SC in the bulk phase. On the other hand, based on the unfavorable miscibility of ST, the intensity of the peak of ST$^{\bullet+}$ decreases drastically due to the incomplete oxidation of ST restricted by the segregation of Li-TFSI in the film. With the increase of Li-salts, as shown in Figure S19c,d, the intensity of specific peaks of spiro-OMeTAD$^{\bullet+}$ and SC$^{\bullet+}$ increases in the same trend. Notably, for ST, the peak of ST$^{\bullet+}$ disappears, accompanied by the red-shift of the absorption edge. Therefore, the properties of ST have changed significantly under the high concentration of dopants, affecting its photovoltaic properties unpredictably.

Based on various structures of molecules, HTMs exhibit different crystallinity and miscibility with dopants. In general, the dopants are prone to aggregate with the evaporation of solvent (CB and *t*-BP) to form precipitations and voids.[55,71] As

https://dx.doi.org/10.1021/acs.chemmater.0c03772
Chem. Mater. XXXX, XXX, XXX–XXX

for SC, because of excellent solubility, a uniform and stable solution can be formed. Then, due to the relatively disordered arrangement of molecules, the amorphous phase of SC would uniformly distribute around dopants to inhibit precipitations of them in the above process. In the case of ST, on account of the poor solubility and high crystallinity, the phase separation between agglomerated dopants and undissolved ST would happen with the removal of the solvent, increasing the number of intrinsic defects during the formation of the film. In parallel, Li-TFSI would be excluded to accumulate around the grain boundaries because of the strong tendency of the formation of ordered regions in ST. As a result, ST has the worst miscibility with dopants among three HTMs, so the film made by it is filled with pinholes. For spiro-OMeTAD, although it possesses less rigid side structures with favorable solubility to suppress phase separation in the early stage, which facilitates the formation of smooth morphology, its eminent crystallinity, similar to ST, also drives the aggregation of dopants during the formation of crystallites. It gives inferior miscibility with Li-salts compared to SC. Consequently, the small size precipitations of Li-salts and voids are observed on the surface. The process of film formation is also displayed in Scheme 1.

To evaluate the performance of HTMs in devices, we fabricated *n-i-p* typed devices with a configuration of FTO/SnO_2/$(CsPbI_3)_x(FAPbI_3)_y(MAPbBr_3)_{1-x-y}$/HTM/Ag, and the structure is displayed in Figure 5a. With the variation of concentration of HTMs and dopants, the optimization processes of device performance are concluded in Tables S2 and S3 and Figures S21 and S22. As the cross-sectional image of the best device with SC given in Figure 5b, the film thickness of SC is about 154 nm which is optimal for its performance. Also, that of ST is similar to SC under the same operation, much thinner than that of spiro-OMeTAD (205 nm) (Figure S20). Under the AM 1.5G illumination, the current density−voltage ($J-V$) curves of the devices with these three HTMs are depicted in Figure 5c,d. All of PSCs expressed small hysteresis based on the same planar device structure. As a control, the device with spiro-OMeTAD gave a desirable PCE of 20.73% with a V_{oc} of 1.12 V, a J_{sc} of 23.84 mA cm^{-2}, and a FF of 77.61%. Also, the device based on SC exhibited the best performance with an encouraging PCE of 21.76%, with a V_{oc} of 1.15 V, a J_{sc} of 23.47 mA cm^{-2}, and a FF of 80.62%. The improved efficiency is a benefit from the enhanced V_{oc} and FF, attributed to the deep HOMO level and good film forming ability of it.[68] On the other hand, with the existence of dense pinholes at the interface, the ST-based device achieved a lower PCE of 18.18% with a V_{oc} of 1.06 V, a J_{sc} of 23.05 mA cm^{-2}, and a FF of 74.39%. Although ST has the deepest HOMO level among three HTMs, the nonradiative recombination of carriers around defects leads to severe V_{oc} loss and poor FF, lowering the efficiencies of devices significantly. The results are summarized in Table 2. Besides, as depicted in Figure 5e, all of devices achieved favorable reproducibility, with average PCEs of 20.03%, 21.04%, and 17.31% for spiro-OMeTAD, SC, and ST, respectively, based on 20 devices.

In addition, the external quantum efficiency (EQE) spectra were characterized to examine the photo responsibility of devices in Figure 5f. The integrated current density values of devices with spiro-OMeTAD, SC, and ST are calculated as 22.87, 22.45, and 21.92 mA cm^{-2}, respectively, which are consistent with the tendency of J_{sc} values measured from $J-V$ curves. Due to the poorest crystallinity and $\pi-\pi$ stacking intensity of SC relatively, it does not exhibit a better capacity

Table 2. Device Photovoltaic Parameters of the Best PSCs with Different HTMs

HTM	scan direction	V_{oc} (V)	J_{sc} (mA cm^{-2})	FF (%)	PCE (%)
spiro-OMeTAD	reverse	1.12	23.84	77.61	20.73
	forward	1.10	23.81	77.49	20.29
SC	reverse	1.15	23.47	80.62	21.76
	forward	1.14	23.47	79.39	21.24
ST	reverse	1.06	23.05	74.39	18.18
	forward	1.04	22.98	72.57	17.35

to transfer holes than spiro-OMeTAD.[63,64] However, with the help of dopants, the intrinsic mobility of SC restricted by weak crystallinity could be improved greatly to achieve a J_{sc} value which is slightly lower than that of spiro-OMeTAD, while maintaining highly enhanced V_{oc} and FF. Moreover, the devices based on SC also gave excellent durability under various concentrations of dopants, exhibiting stable performance (Table S3). Notably, compared to SC, due to the inferior film forming ability derived from poor miscibility with Li-TFSI of ST, the dense pinholes in ST reduced the effective contact area with the active layer and the electrodes so as to decrease the efficiency of hole extraction, resulting in the drop-off of J_{sc} value which is the lowest among devices based on three HTMs. Meanwhile, its device performance is affected drastically with the variation of doping concentration, thus it is difficult to find a balance to optimize the ST-based devices (Table S3). Conclusively, the strong crystallinity of molecules could expedite the formation of defects, bringing passive effects to the performance of devices although the enhanced mobility could be accomplished. Hence, as for the design of novel spiro-typed HTM with dopants, the morphology of the film plays a dominant role in eliminating defects to promote device properties comprehensively; besides, a deep HOMO level should be required for building large V_{oc}.

To further investigate the process of hole extraction at the interface between perovskite and HTMs, steady-state photoluminescence (PL) and time-resolved photoluminescence (TRPL) measurements were performed. Figure 6a depicts that the pristine perovskite film exhibits an evident emission peak around 790 nm. With the coverage of HTMs on the perovskite, the intensity of emission is quenched remarkably, expressing their strong capacity of hole extraction at the interface. In sequence, the perovskite coated with spiro-OMeTAD, SC, and ST could reduce the initial intensity to 0.90%, 1.31%, and 2.14%, respectively, reflecting their hole extraction ability from strong to weak, in agreement with the change of J_{sc} values. Furthermore, the PL decaying curves are fitted by a biexponential equation,[40,72] in which the fast decay (τ_1) represents the carrier extraction to the HTMs primarily, while the second slow decay (τ_2) mainly reflects interface recombination losses[45] (Figure 6b). The fitting parameters are listed in Table S4, and the short lifetime represents the higher efficiency of hole extraction. Compared to perovskite/spiro-OMeTAD bilayer (τ_1 = 1.17 ns, τ_2 = 9.65 ns), perovskite/SC film exhibits a shorter lifetime (τ_1 = 0.94 ns, τ_2 = 7.31 ns) because of the improved interfacial contact and smoother morphology, showing more efficient hole extraction and reduced nonradiative recombination which contributes to high V_{oc} and FF. On the other hand, because of the pinholes, the hole extraction efficiency of ST is cut down and performs a slightly longer lifetime (τ_1 = 1.38 ns, τ_2 = 10.01 ns) than those

https://dx.doi.org/10.1021/acs.chemmater.0c03772
Chem. Mater. XXXX, XXX, XXX−XXX

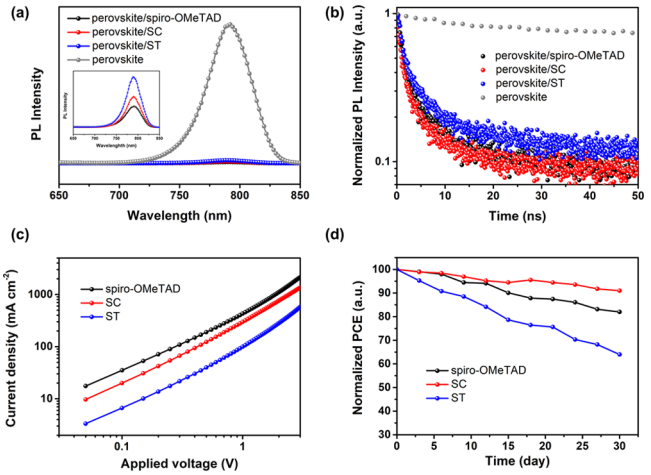

Figure 6. (a) Steady-state PL spectra and (b) time-resolved PL spectra of pristine perovskite films, perovskite coated with spiro-OMeTAD, SC, and ST, respectively. (c) Hole mobility measurement of three doped HTMs through space-charge-limited-current (SCLC) analysis. (d) Long-term stability of devices based on three HTMs without encapsulation (under 25 °C, 30 ± 5% relative humidity).

of the first two, exhibiting lower hole extraction ability and enhanced nonradiative recombination. Therefore, as a benefit of the neat film morphology of the interface primarily, the film of SC expresses the highest efficiency to extract holes.

Moreover, based on the space-charge-limited-current (SCLC) model, the hole mobility of HTMs with dopants was estimated by the hole-only device of ITO/PEDOT:PSS/HTM/MoO_3/Ag under dark conditions.[63] The current density−voltage (J−V) curves are shown in Figure 6c. The values of hole mobility are calculated with the Mott−Gurney equation, concluded in Table 1. Corresponding to the variation of crystallinity of HTMs, the mobility values of spiro-OMeTAD and SC are calculated to be 5.88×10^{-3} cm^2 V^{-1} s^{-1} and 3.15×10^{-3} cm^2 V^{-1} s^{-1}, respectively. Notably, the mobility of ST is the lowest among three HTMs (1.77×10^{-3} cm^2 V^{-1} s^{-1}), ascribed to the poor miscibility with Li-TFSI and problematic interfacial contacts caused by pinholes. With suitable hole mobility, both spiro-OMeTAD and SC could extract holes from the perovskite efficiently. The distinction of hole mobility among HTMs is also consistent with the results from PL and EQE tests.

To evaluate the long-term stability of devices with different HTMs, the water contact angles of spiro-OMeTAD, SC, and ST based on the solid substrate were estimated to assess their hydrophobicity. The results are measured as 81.6°, 89.0°, and 89.6°, respectively. As shown in Figure S23a, SC and ST exhibit better hydrophobicity because of the higher ratio of rigid and hydrophobic moieties in molecules, inhibiting the contact of moisture with perovskite effectively, as compared to spiro-OMeTAD. In addition, the stability of devices is determined by the morphology of HTMs and the presence of Li-salts. Inside HTMs, the incorporation of dopants, such as Li-TFSI, could also capture moisture in humid conditions easily and accelerate the decomposition rate of perovskite, causing irreversible damage to the stability of devices. For spiro-OMeTAD, the precipitations of Li-salts are visible on the surface. In the case of ST, the defects appear as voids, providing opportunities for the permeation of moisture into perovskite and expediting the formation of AgI between perovskite and silver electrodes thus reducing the stability of PSCs drastically.[37,73,74] None of the defects are apparent on the surface of SC from previous characterizations. Next, the long-term stability of PSCs was examined without encapsulation in the ambient conditions (temperature, 25 °C; relative humidity, 30 ± 5%) and depicted in Figure 6d. After 30 days, the device based on SC can still keep a PCE retention over 90% of the initial value, while that of spiro-OMeTAD maintained 82% of the original value under the same conditions. Meanwhile, the solar cell based on ST only sustained 64% of the original PCE. Moreover, the SC-based device performed superior thermal stability under 60 °C in a glovebox with N_2, retaining about 87% of the initial PCE after 500 h, whereas the PCEs of spiro-OMeTAD-based and ST-based device was dropped to 69% and 63% of initial values at that time, respectively. Additionally, the thermal stability test was also carried out under 60 °C with a relative humidity of 30 ± 5%, and the device with SC could still preserve 68% of original PCE after 500 h. In contrast, the PCE of the device based on spiro-OMeTAD was reduced to only 42%, while the device with ST lost performance completely in such a condition (Figure S23b,c). Furthermore, in Figure S24, the decomposition rate of perovskite covered by different HTMs was measured to evaluate the stability of devices. In a harsh environment (temperature, 60 °C; relative humidity, 85 ± 5%), the perovskite with ST started to tarnish only after 1 d, while that covered by spiro-OMeTAD and SC can keep initial states for 3 days and 4 days, respectively. Finally, the time of total decomposition of perovskite was measured as 7 days, 10 days, and 3 days for spiro-OMeTAD, SC, and ST, respectively. Therefore, SC not only endows devices with high efficiency but gives excellent thermal and humid durability, ascribed to uniform morphology, large molecular weight, and hydrophobic structures. Besides, the reasonable modification of side groups in spiro-typed HTMs could promote the thermal and humid stability of PSCs effectively as well.

CONCLUSION

In conclusion, we have synthesized two spiro-typed HTMs, SC and ST modified by *N*-ethylcarbazole and dibenzothiophene, respectively. With the existence of alkyl chains, SC obtains reduced $\pi-\pi$ stacking, low crystallinity, and enhanced solubility, resulting in impressive miscibility with dopants to form a homogeneous morphology of the surface without visible defects. Besides, the extended π-conjugated structures contribute to the establishment of the deep HOMO level which could enhance the V_{oc} of the devices. Thus, the device based on SC shows the best performance with a PCE value of 21.76%, attributed to the evident promotion of V_{oc} (1.15 V) and FF (80.62%). Meanwhile, with the increase of molecular weight and hydrophobicity of SC, the device also gives desirable long-term stability, maintaining over 90% of initial efficiency for more than 30 days without encapsulation in ambient air. It also performs favorable thermal and humid durability, exhibiting better performance than that of spiro-OMeTAD comprehensively. In contrast, due to low solubility and high crystallinity, the film of doped ST is filled with small pinholes which lead to severe V_{oc} loss (1.06 V), low FF (74.39%), much lower efficiency (18.18%), and inferior stability of device than those of the other two HTMs. Therefore, we demonstrate that the morphology of HTMs plays a dominant role in determining the performance of PSCs, and we believe that this strategy of molecular design is

https://dx.doi.org/10.1021/acs.chemmater.0c03772
Chem. Mater. XXXX, XXX, XXX−XXX

instructive to improve device performance with spiro-typed HTMs in the future.

EXPERIMENTAL SECTION

Materials. 2-Bromocarbazole (98%), 4-methoxyaniline (98%), and 2,2′,7,7′-tetrabromo-9,9′-spirobi[fluorene] (98%) were purchased from Aladdin. P(*t*-Bu)$_3$ (1 M solution in toluene), potassium hydroxide (98%), and NaO^{t}Bu (98%) were purchased from Macklin. Pd$_2$(dba)$_3$ (97%) and 2-bromodibenzo[*b*, *d*]thiophene (98%) were purchased from Accela. Anhydrous and oxygen-free solvents were obtained with calcium hydride reflux. Fluorine-doped tin oxide (FTO) glass substrates with a sheet resistance of 7 Ω/sq were purchased from Liaoninghuite Co., Ltd. SnO_2 colloid precursor (tin(IV) oxide, 15% in H_2O colloidal dispersion) was obtained from Alfa Aesar. *N*, *N*-dimethylformamide (DMF, 99.8%), dimethyl sulfoxide (DMSO 99.8%), and chlorobenzene (99.9%) were acquired from Sigma-Aldrich. Isopropanol (IPA, 99.8%) was purchased from Innochem. Lead(II) iodide (PbI_2, 99.8%) was purchased from Kanto Chemical. 2,2′,7,7′-tetrakis(*N*,*N*-di-*p*-methoxyphenylamine)-9,9′-spirobifuorene (spiro-OMeTAD, 99%), lithium bis-(trifluoromethylsulfonyl) imide (Li-TFSI, 95%), and 4-*tert*-butylpyridine (*t*-BP, 96%) were obtained from Lumtec. Lead(II) iodide (PbI_2, 99.8%), formamidinium iodide (FAI, 99.5%), methylammonium bromide (MABr, 99.5%), methylamine chloride (MACl, 99.5%), methylamine iodide (MAI, 99.5%), and cesium iodide (CsI, 99.8%) were acquired from Xi'an Polymer Light Technology. All materials were used without any further purification.

Synthesis of 2-Bromo-9-ethyl-9H-carbazole. In a dry 100 mL two-necked flask, 2-bromocarbazole (2.0 g, 8.13 mmol) and potassium hydroxide (1.37 g, 24.38 mmol) were dissolved into 40 mL of acetone. The mixture was heated to reflux under an argon atmosphere for 30 min. Then, ethyl bromide (1.77 g, 16.25 mmol) was added slowly and reflux continued for 1 h. After cooling to room temperature, the mixture was washed with 2% dilute hydrochloric acid, saturated $NaHCO_3$ aqueous solution and water successively. The organic layer was dried over anhydrous Na_2SO_4. After removal of solvent, the crude material was purified by column chromatography (CH_2Cl_2/petroleum ether, 1/10 v/v) to afford a product as a white crystal (yield: 2.02 g, 90.6%).[58] ^{1}H NMR (400 MHz, $CDCl_3$): δ 1.43 (t, 3H), 4.32 (q, 2H), 7.24 (dd, 1H), 7.34 (dd, 1H), 7.41 (d, 1H), 7.50 (m, 1H), 7.56 (d, 1H), 7.94 (d, 1H), 8.07 (d, 1H). ^{13}C NMR (500 MHz, $CDCl_3$): δ 13.88, 37.79, 108.79, 111.68, 119.37, 119.47, 120.55, 121.67, 122.02, 122.05, 122.56, 126.20, 140.19, 140.89.

Synthesis of 9-Ethyl-*N*-(4-methoxyphenyl)-9*H*-carbazol-2-amine (1). In a dry 100 mL two-necked flask, 2-bromo-9-ethyl-9H-carbazole (2.0 g, 7.30 mmol), 4-methoxyaniline (1.35 g, 10.94 mmol), Pd$_2$(dba)$_3$ (0.335 g, 0.366 mmol), P(*t*-Bu)$_3$ (0.118 g, 0.585 mmol), and NaO^{t}Bu (1.576 g, 16.40 mmol) were dissolved into 30 mL of toluene. The mixture was heated at 110 °C for 24 h under argon atmosphere. After cooling to room temperature, the mixture was washed with brine water. The organic layer was dried over anhydrous Na_2SO_4. After removal of solvent, the crude material was purified by column chromatography (ethyl acetate/petroleum ether, 1/5 v/v) to afford a product as a pale yellow solid (yield: 1.34 g, 58.1%). ^{1}H NMR (400 MHz, DMSO-d_6): δ 1.27 (t, 3H), 3.73 (s, 3H), 4.27 (q, 2H), 6.82 (dd, 1H), 6.90 (d, 2H), 7.00 (d, 1H), 7.10 (t, 1H), 7.15 (d, 2H), 7.29 (t, 1H), 7.46 (d, 1H), 7.89 (d, 1H), 7.93 (d, 1H), 8.05 (s, 1H). ^{13}C NMR (500 MHz, DMSO-d_6): δ 13.49, 36.71, 55.22, 93.71, 108.42, 109.04, 114.61, 114.69, 118.53, 118.77, 120.08, 121.06, 122.89, 123.66, 136.54, 139.41, 141.08, 144.04, 153.70.

Synthesis of N^2,$N^{2\prime}$,N^7,$N^{7\prime}$-tetrakis(9-ethyl-9*H*-carbazol-2-yl)-N^2,$N^{2\prime}$,N^7,$N^{7\prime}$-tetrakis(4-methoxyphenyl)-9,9′-spirobi-[fluorene]-2,2′,7,7′-tetraamine (SC). In a dry 100 mL two-necked flask, 2,2′,7,7′-tetrabromo-9,9′-spirobi[fluorene] (0.4 g, 0.633 mmol), 9-ethyl-*N*-(4-methoxyphenyl)-9*H*-carbazol-2-amine (1.0 g, 3.16 mmol), Pd$_2$(dba)$_3$ (57.8 mg, 0.063 mmol), P(*t*-Bu)$_3$ (25.5 mg. 0.126 mmol), and NaO^{t}Bu (0.395 g, 4.108 mmol) were dissolved into 25 mL of toluene. The mixture was heated at 120 °C for 24 h under argon atmosphere. After cooling to room temperature, the mixture was washed with brine water. The organic layer was dried over anhydrous Na_2SO_4. After removal of solvent, the crude material was purified by column chromatography (tetrahydrofuran/petroleum ether, 1/3 v/v) to afford a product as a pale yellow solid (yield: 0.514 g, 51.6%). ^{1}H NMR (400 MHz, DMSO-d_6): δ 1.12 (t, 12H), 3.74 (s, 12H), 4.14 (q, 8H), 6.48 (d, 4H), 6.71 (dd, 4H), 6.78 (dd, 4H), 6.86 (d, 8H), 6.98 (d, 8H), 7.03 (d, 4H), 7.16 (t, 4H), 7.36 (t, 4H), 7.47 (t, 8H), 7.91 (d, 4H), 8.01 (d, 4H). ^{13}C NMR (500 MHz, DMSO-d_6): δ 14.04, 37.26, 55.66, 65.72, 103.60, 109.34, 115.30, 115.73, 116.72, 118.15, 119.38, 120.11, 120.91, 121.41, 122.24, 122.60, 125.37, 127.07, 134.92, 140.36, 140.79, 146.23, 147.51, 149.84, 156.20. MS (MALDI-TOF) *m*/*z*: calculated for $C_{109}H_{88}N_8O_4$, $[M]^+$, 1573.9550; found 1573.6160.

Synthesis of *N*-(4-Methoxyphenyl)dibenzo[*b*,*d*]thiophen-2-amine (2). In a dry 100 mL two-necked flask, 2-bromodibenzo[*b*, *d*]thiophene (2.0 g, 7.60 mmol), 4-methoxyaniline (1.404 g, 11.40 mmol), Pd$_2$(dba)$_3$ (0.348 g, 0.380 mmol), P(*t*-Bu)$_3$ (0.123 g, 0.608 mmol), and NaO^{t}Bu (1.643 g, 17.1 mmol) were dissolved into 30 mL of toluene. The mixture was heated at 110 °C for 24 h under argon atmosphere. After cooling to room temperature, the mixture was washed with brine water. The organic layer was dried over anhydrous Na_2SO_4. After removal of solvent, the crude material was purified by column chromatography (ethyl acetate/petroleum ether, 1/5 v/v) to afford a product as a white solid (yield: 1.49g, 64.2%). ^{1}H NMR (400 MHz, DMSO-d_6): δ 3.74 (s, 3H), 6.91 (d, 2H), 7.14 (m, 3H), 7.45 (m, 2H), 7.79 (m, 2H), 7.95 (d, 1H), 8.07 (s, 1H), 8.14 (d, 1H). ^{13}C NMR (500 MHz, DMSO-d_6): δ 55.23, 106.62, 114.67, 117.31, 120.07, 121.71, 123.06, 123.49, 124.38, 126.78, 128.13, 134.89, 135.96, 136.44, 139.47, 142.95, 153.83.

Synthesis of N^2,$N^{2\prime}$,N^7,$N^{7\prime}$-Tetrakis(dibenzo[*b*,*d*]thiophen-2-yl)-N^2,$N^{2\prime}$,N^7,$N^{7\prime}$-tetrakis(4-methoxyphenyl)-9,9′-spirobi-[fluorene]-2,2′,7,7′-tetraamine (ST). In a dry 100 mL two-necked flask, 2,2′,7,7′-tetrabromo-9,9′-spirobi[fluorene] (0.414 g, 0.655 mmol), *N*-(4-methoxyphenyl)dibenzo[*b*, *d*]thiophen-2-amine (1.0 g, 3.275 mmol), Pd$_2$(dba)$_3$ (60.0 mg, 0.0655 mmol), P(*t*-Bu)$_3$ (26.5 mg. 0.131 mmol), and NaO^{t}Bu (0.409 g, 4.258 mmol) were dissolved into 25 mL of toluene. The mixture was heated at 120 °C for 24 h under an argon atmosphere. After cooling to room temperature, the mixture was washed with brine water. The organic layer was dried over anhydrous Na_2SO_4. After removal of solvent, the crude material was purified by column chromatography (tetrahydrofuran/petroleum ether, 1/3 v/v) to afford a product as a pale yellow solid (yield: 0.498 g, 49.7%). ^{1}H NMR (400 MHz, DMSO-d_6): δ 3.73 (s, 12H), 6.43 (d, 4H), 6.78 (d, 4H), 6.86 (d, 8H), 6.96 (d, 8H), 7.01 (d, 4H), 7.34 (t, 4H), 7.44 (t, 8H), 7.80 (d, 8H), 7.97 (t, 8H). ^{13}C NMR (500 MHz, DMSO-d_6): δ 55.62, 65.69, 115.34, 116.51, 116.63, 121.00, 122.05, 122.27, 123.52, 123.89, 124.10, 124.96, 126.98, 127.55, 132.99, 134.94, 135.01, 136.61, 139.88, 140.49, 145.38, 147.34, 149.89, 156.25. MS (MALDI-TOF) *m*/*z*: calculated for $C_{101}H_{68}N_4O_4S_4$, $[M]^+$, 1529.9190; found 1529.3330.

Devices Fabrication. FTO glass substrates were cleaned ultrasonically in ethyl alcohol, detergent, deionized water, acetone, and isopropyl alcohol each for 15 min, sequentially. Prior to use, the FTO substrates were treated with UV−ozone for 25 min. Then, the diluted SnO_2 colloid precursor (2.67%, in water) was spin-coated onto FTO substrates at 3000 rpm for 30 s and annealed on a hot plate at 150 °C for 30 min. After cooling to room temperature, the FTO/SnO_2 substrates were treated with UV ozone again for 25 min. Subsequently, the perovskite layer was prepared through a two-step method. First, 600 mg of PbI_2, 30 mg of CsI, and 6.4 mg of MAI in 1 mL of DMF/DMSO (9:1) solution was spin-coated on the SnO_2 substrate at 1500 rpm for 30 s, then the samples were annealed at 70 °C for 1 min. Subsequently, 60 mg of FAI, 6 mg of MABr, and 6 mg of MACl in 1 mL of IPA solution was spin-coated onto the PbI_2 film at 1500 rpm for 30 s, and then the perovskite was annealed at 150 °C for 20 min in ambient air conditions (25−30% humidity). For the deposition of hole transporting layers, 72.3 mg of spiro-OMeTAD with the addition of 54 μL of Li-TFSI (170 mg/mL in acetonitrile) and 30 μL of *t*-BP were dissolved into 1 mL of chlorobenzene, and the solution was spin-coated on perovskite at 3000 rpm for 30 s.

https://dx.doi.org/10.1021/acs.chemmater.0c03772
Chem. Mater. XXXX, XXX, XXX−XXX

Meanwhile, the optimized concentration in 1 mL of chlorobenzene was found to be 46.3 mg for SC and ST. In addition, 30 μL of *t*-BP, Li-TFSI solution (170 mg/mL in acetonitrile) was added as 54 μL into the solution. The solution of novel HTMs was spin-coated onto the perovskite at 2000 rpm for 30 s. Finally, Ag back electrodes (100 nm) were deposited by thermal evaporation under 1×10^{-5} Torr pressure. The accurate active area was 0.1 cm^2 defined by a nonreflective mask.

Materials Characterization. ^1H and ^{13}C NMR spectra were measured on a Bruker AVANCE III HD 400 and AVANCE III HD 500 spectrometer with $CDCl_3$ and DMSO-d_6. Matrix-assisted laser desorption-ionization-time-of-flight (MALDI-TOF) mass spectra were recorded on a Bruker auto flex Speed TOF. The UV−vis absorption spectra were collected on a Lambda 750S spectrophotometer based on solid state films. Cyclic voltammetry (CV) measurements were performed on a CHI604E electrochemical workstation, consisting of a platinum working electrode, a platinum sheet counter electrode, and an Ag/Ag^+ as the reference electrode. HTMs were dissolved into anhydrous CH_2Cl_2, containing 0.1 M *n*-Bu_4NPF_6 as electrolyte. The scan rate was 100 mV s^{-1}, and all calculated potentials were calibrated with ferrocene/ferrocenium (Fc/Fc^+) as reference. Density functional theory (DFT) calculations were performed by the Gaussian 09 program at the B3LYP/6-31G (d) level. Ultraviolet photoelectron spectroscopy (UPS) was characterized by *1/AXIS UltraDLD. TGA was performed with a Pyris 1 TGA with the heating rate of 10 °C min^{-1} under N_2 atmosphere, and DSC curves were recorded on a DSC 2500 under the same conditions. The Grazing incidence wide-angle X-ray scattering (GIWAXS) data were obtained at beamline BL16B1 of the Shanghai Synchrotron Radiation Facility (SSRF) using X-ray with a wavelength of 1.24 Å.

Devices Characterization. SEM images were performed by a TESCAN MAIA3 GMU model 2016 scanning electron microscope. Topographic AFM images were obtained by a Bruker Multimode 8 operated in tapping mode under ambient conditions. The contact angles of three HTMs in solid state were measured by DSA100. The spectra of TOF-SIMS were obtained by a GAIA3 GMU model 2016 scanning electron microscope. TRPL and steady state PL spectra were measured on a FLS1000 photoluminescence spectrometer with an excitation wavelength of 470 nm. The current density−voltage (*J*−*V*) curves were measured by an Abet Technologies Sun 2000 solar simulator under AM 1.5G illumination at 100 mW cm^{-2}. The light intensity was calibrated with a standard VLSI Si reference solar cell (SRC-1000-TC-K-QZ). The devices were masked with an aperture area of 0.1 cm^2 without encapsulation. EQE spectra were recorded with an Enlitech LQE-50-FLIPCE measurement system.

■ ASSOCIATED CONTENT

Supporting Information

The Supporting Information is available free of charge at https://pubs.acs.org/doi/10.1021/acs.chemmater.0c03772.

Synthetic routes of SC and ST; the method of hole mobility measurements; the details of stability test of devices; ^1H and ^{13}C NMR and MALDI-TOF spectra of the developed compounds; UPS spectra of perovskite and HTMs; TGA and DSC tests of HTMs; DFT result of spiro-OMeTAD; top view SEM images, AFM images, and cross-sectional SEM images of devices; TOF-SIMS mappings of the distribution of dopants in HTMs; UV−vis spectra of radical cation; the devices performance under various concentrations of HTMs and dopants; contact angle of HTMs in the solid state and the stability tests of devices; decomposition rate of perovskite coated by HTMs; and cost calculations (PDF)

■ AUTHOR INFORMATION

Corresponding Author

Chun-Chao Chen − *School of Materials Science and Engineering, Shanghai Jiao Tong University, Shanghai 200240, China;* orcid.org/0000-0002-3541-4348; Email: c3chen@sjtu.edu.cn

Authors

Zihao Deng − *School of Materials Science and Engineering, Shanghai Jiao Tong University, Shanghai 200240, China*

Maosheng He − *School of Materials Science and Engineering, Shanghai Jiao Tong University, Shanghai 200240, China*

Yi Zhang − *School of Chemistry and Chemical Engineering, Shanghai Jiao Tong University, Shanghai 200240, China*

Fateh Ullah − *School of Materials Science and Engineering, Shanghai Jiao Tong University, Shanghai 200240, China*

Kui Ding − *School of Chemistry and Chemical Engineering, Shanghai Jiao Tong University, Shanghai 200240, China*

Jianghu Liang − *School of Materials Science and Engineering, Shanghai Jiao Tong University, Shanghai 200240, China*

Zhanfei Zhang − *School of Materials Science and Engineering, Shanghai Jiao Tong University, Shanghai 200240, China*

Heng Xu − *School of Materials Science and Engineering, Shanghai Jiao Tong University, Shanghai 200240, China*

Yuankun Qiu − *School of Materials Science and Engineering, Shanghai Jiao Tong University, Shanghai 200240, China*

Ziyi Xie − *School of Chemistry and Chemical Engineering, Shanghai Jiao Tong University, Shanghai 200240, China*

Tong Shan − *School of Chemistry and Chemical Engineering, Shanghai Jiao Tong University, Shanghai 200240, China;* orcid.org/0000-0001-5695-2543

Zhenhua Chen − *Shanghai Synchrotron Radiation Facility (SSRF), Shanghai Advanced Research Institute, Chinese Academy of Sciences, Shanghai 201800, China*

Hongliang Zhong − *School of Chemistry and Chemical Engineering, Shanghai Jiao Tong University, Shanghai 200240, China;* orcid.org/0000-0003-2499-8007

Complete contact information is available at: https://pubs.acs.org/10.1021/acs.chemmater.0c03772

Author Contributions

All authors have given approval to the final version of the manuscript.

Notes

The authors declare no competing financial interest.

■ ACKNOWLEDGMENTS

This work was funded by National Natural Science Foundation of China (Grant No. 51950410581), Shanghai Pujiang Program, and Open Fund of Zhejiang Tsinghua Institute of Flexible Electronics Technology. H.Z. acknowledges funding from National Natural Science Foundation of China (Grant No. 21604053). The authors thank the support from staff of beamline BL16B1 in the Shanghai Synchrotron Radiation Facility (SSRF) for sample characterization.

■ REFERENCES

(1) Rong, Y.; Hu, Y.; Mei, A.; Tan, H.; Saidaminov, M. I.; Seok, S. Il; McGehee, M. D.; Sargent, E. H.; Han, H. Challenges for Commercializing Perovskite Solar Cells. *Science* **2018**, *361*, No. eaat8235.

(2) Wang, L.; Wang, X.; Deng, L. L.; Leng, S.; Guo, X.; Tan, C. H.; Choy, W. C. H.; Chen, C. C. The Mechanism of Universal Green

Antisolvents for Intermediate Phase Controlled High-Efficiency Formamidinium-Based Perovskite Solar Cells. *Mater. Horiz.* **2020**, *7*, 934−942.
(3) Kojima, A.; Teshima, K.; Shirai, Y.; Miyasaka, T. Organometal Halide Perovskites as Visible-Light Sensitizers for Photovoltaic Cells. *J. Am. Chem. Soc.* **2009**, *131*, 6050−6051.
(4) Kim, H. S.; Lee, C. R.; Im, J. H.; Lee, K. B.; Moehl, T.; Marchioro, A.; Moon, S. J.; Humphry-Baker, R.; Yum, J. H.; Moser, J. E.; Grätzel, M.; Park, N. G. Lead Iodide Perovskite Sensitized All-Solid-State Submicron Thin Film Mesoscopic Solar Cell with Efficiency Exceeding 9%. *Sci. Rep.* **2012**, *2*, 591.
(5) Liu, M.; Johnston, M. B.; Snaith, H. J. Efficient Planar Heterojunction Perovskite Solar Cells by Vapour Deposition. *Nature* **2013**, *501*, 395−398.
(6) Aguiar, J. A.; Wozny, S.; Holesinger, T. G.; Aoki, T.; Patel, M. K.; Yang, M.; Berry, J. J.; Al-Jassim, M.; Zhou, W.; Zhu, K. In Situ Investigation of the Formation and Metastability of Formamidinium Lead Tri-Iodide Perovskite Solar Cells. *Energy Environ. Sci.* **2016**, *9*, 2372−2382.
(7) Jiang, Q.; Zhao, Y.; Zhang, X.; Yang, X.; Chen, Y.; Chu, Z.; Ye, Q.; Li, X.; Yin, Z.; You, J. Surface Passivation of Perovskite Film for Efficient Solar Cells. *Nat. Photonics* **2019**, *13*, 460−466.
(8) *NREL Efficiency Chart*, https://www.nrel.gov/pv/assets/pdfs/best-research-cell-efficiencies.20190802.pdf (accessed 08-2019).
(9) D'Innocenzo, V.; Grancini, G.; Alcocer, M. J. P.; Kandada, A. R. S.; Stranks, S. D.; Lee, M. M.; Lanzani, G.; Snaith, H. J.; Petrozza, A. Excitons versus Free Charges in Organo-Lead Tri-Halide Perovskites. *Nat. Commun.* **2014**, *5*, 3586.
(10) Green, M. A.; Ho-Baillie, A.; Snaith, H. J. The Emergence of Perovskite Solar Cells. *Nat. Photonics* **2014**, *8*, 506−514.
(11) Jiang, Q.; Chu, Z.; Wang, P.; Yang, X.; Liu, H.; Wang, Y.; Yin, Z.; Wu, J.; Zhang, X.; You, J. Planar-Structure Perovskite Solar Cells with Efficiency beyond 21%. *Adv. Mater.* **2017**, *29*, 1703852.
(12) Jiang, Q.; Zhang, L.; Wang, H.; Yang, X.; Meng, J.; Liu, H.; Yin, Z.; Wu, J.; Zhang, X.; You, J. Enhanced Electron Extraction Using SnO2 for High-Efficiency Planar-Structure HC(NH2)2 PbI3-Based Perovskite Solar Cells. *Nat. Energy* **2017**, *2*, 16177.
(13) Nie, W.; Tsai, H.; Asadpour, R.; Blancon, J.-C.; Neukirch, A. J.; Gupta, G.; Crochet, J. J.; Chhowalla, M.; Tretiak, S.; Alam, M. A.; Wang, H.-L.; Mohite, A. D. High-Efficiency Solution-Processed Perovskite Solar Cells with Millimeter-Scale Grains. *Science* **2015**, *347*, 522−526.
(14) Yang, D.; Yang, R.; Ren, X.; Zhu, X.; Yang, Z.; Li, C.; Liu, S. F. Hysteresis-Suppressed High-Efficiency Flexible Perovskite Solar Cells Using Solid-State Ionic-Liquids for Effective Electron Transport. *Adv. Mater.* **2016**, *28*, 5206−5213.
(15) Yang, W. S.; Park, B. W.; Jung, E. H.; Jeon, N. J.; Kim, Y. C.; Lee, D. U.; Shin, S. S.; Seo, J.; Kim, E. K.; Noh, J. H.; Seok, S., II Iodide Management in Formamidinium-Lead-Halide-Based Perovskite Layers for Efficient Solar Cells. *Science* **2017**, *356*, 1376−1379.
(16) Yin, W. J.; Shi, T.; Yan, Y. Unique Properties of Halide Perovskites as Possible Origins of the Superior Solar Cell Performance. *Adv. Mater.* **2014**, *26*, 4653−4658.
(17) Di Giacomo, F.; Fakharuddin, A.; Jose, R.; Brown, T. M. Progress, Challenges and Perspectives in Flexible Perovskite Solar Cells. *Energy Environ. Sci.* **2016**, *9*, 3007−3035.
(18) Heo, J. H.; Im, S. H.; Noh, J. H.; Mandal, T. N.; Lim, C. S.; Chang, J. A.; Lee, Y. H.; Kim, H. J.; Sarkar, A.; Nazeeruddin, M. K.; Grätzel, M.; Seok, S., II Efficient Inorganic-Organic Hybrid Heterojunction Solar Cells Containing Perovskite Compound and Polymeric Hole Conductors. *Nat. Photonics* **2013**, *7*, 486−491.
(19) Jeng, J. Y.; Chiang, Y. F.; Lee, M. H.; Peng, S. R.; Guo, T. F.; Chen, P.; Wen, T. C. CH3NH3PbI3 Perovskite/Fullerene Planar-Heterojunction Hybrid Solar Cells. *Adv. Mater.* **2013**, *25*, 3727−3732.
(20) Li, Z.; Zhu, Z.; Chueh, C. C.; Jo, S. B.; Luo, J.; Jang, S. H.; Jen, A. K. Y. Rational Design of Dipolar Chromophore as an Efficient Dopant-Free Hole-Transporting Material for Perovskite Solar Cells. *J. Am. Chem. Soc.* **2016**, *138*, 11833−11839.
(21) You, J.; Meng, L.; Song, T.-B.; Guo, T.-F.; Yang, Y.; Chang, W.-H.; Hong, Z.; Chen, H.; Zhou, H.; Chen, Q.; Liu, Y.; De Marco, N.; Yang, Y. Improved Air Stability of Perovskite Solar Cells via Solution-Processed Metal Oxide Transport Layers. *Nat. Nanotechnol.* **2016**, *11*, 75−81.
(22) Yu, Z.; Sun, L. Recent Progress on Hole-Transporting Materials for Emerging Organometal Halide Perovskite Solar Cells. *Adv. Energy Mater.* **2015**, *5*, 1500213.
(23) Qin, P.; Tanaka, S.; Ito, S.; Tetreault, N.; Manabe, K.; Nishino, H.; Nazeeruddin, M. K.; Grätzel, M. Inorganic Hole Conductor-Based Lead Halide Perovskite Solar Cells with 12.4% Conversion Efficiency. *Nat. Commun.* **2014**, *5*, 3834.
(24) Xu, B.; Sheibani, E.; Liu, P.; Zhang, J.; Tian, H.; Vlachopoulos, N.; Boschloo, G.; Kloo, L.; Hagfeldt, A.; Sun, L. Carbazole-Based Hole-Transport Materials for Efficient Solid-State Dye-Sensitized Solar Cells and Perovskite Solar Cells. *Adv. Mater.* **2014**, *26*, 6629−6634.
(25) Yang, W. S.; Noh, J. H.; Jeon, N. J.; Kim, Y. C.; Ryu, S.; Seo, J.; Seok, S., II High-Performance Photovoltaic Perovskite Layers Fabricated through Intramolecular Exchange. *Science* **2015**, *348*, 1234−1237.
(26) Bakr, Z. H.; Wali, Q.; Fakharuddin, A.; Schmidt-Mende, L.; Brown, T. M.; Jose, R. Advances in Hole Transport Materials Engineering for Stable and Efficient Perovskite Solar Cells. *Nano Energy* **2017**, *34*, 271−305.
(27) Bai, Y.; Meng, X.; Yang, S. Interface Engineering for Highly Efficient and Stable Planar P-i-n Perovskite Solar Cells. *Adv. Energy Mater.* **2018**, *8*, 1701883.
(28) Urieta-Mora, J.; García-Benito, I.; Molina-Ontoria, A.; Martín, N. Hole Transporting Materials for Perovskite Solar Cells: A Chemical Approach. *Chem. Soc. Rev.* **2018**, *47*, 8541−8571.
(29) Rakstys, K.; Igci, C.; Nazeeruddin, M. K. Efficiency: Vs. Stability: Dopant-Free Hole Transporting Materials towards Stabilized Perovskite Solar Cells. *Chem. Sci.* **2019**, *10*, 6748−6769.
(30) Zhang, F.; Yi, C.; Wei, P.; Bi, X.; Luo, J.; Jacopin, G.; Wang, S.; Li, X.; Xiao, Y.; Zakeeruddin, S. M.; Grätzel, M. A Novel Dopant-Free Triphenylamine Based Molecular "Butterfly" Hole-Transport Material for Highly Efficient and Stable Perovskite Solar Cells. *Adv. Energy Mater.* **2016**, *6*, 1600401.
(31) Zhang, J.; Zhang, T.; Jiang, L.; Bach, U.; Cheng, Y. B. 4- Tert-Butylpyridine Free Hole Transport Materials for Efficient Perovskite Solar Cells: A New Strategy to Enhance the Environmental and Thermal Stability. *ACS Energy Lett.* **2018**, *3*, 1677−1682.
(32) Liu, F.; Li, Q.; Li, Z. Hole-Transporting Materials for Perovskite Solar Cells. *Asian J. Org. Chem.* **2018**, *7*, 2182−2200.
(33) Kasparavicius, E.; Magomedov, A.; Malinauskas, T.; Getautis, V. Long-Term Stability of the Oxidized Hole-Transporting Materials Used in Perovskite Solar Cells. *Chem. - Eur. J.* **2018**, *24*, 9910−9918.
(34) Hawash, Z.; Ono, L. K.; Qi, Y. Recent Advances in Spiro-MeOTAD Hole Transport Material and Its Applications in Organic-Inorganic Halide Perovskite Solar Cells. *Adv. Mater. Interfaces* **2018**, *5*, 1700623.
(35) Cappel, U. B.; Daeneke, T.; Bach, U. Oxygen-Induced Doping of Spiro-MeOTAD in Solid-State Dye-Sensitized Solar Cells and Its Impact on Device Performance. *Nano Lett.* **2012**, *12*, 4925−4931.
(36) Song, Z.; Abate, A.; Watthage, S. C.; Liyanage, G. K.; Phillips, A. B.; Steiner, U.; Graetzel, M.; Heben, M. J. Perovskite Solar Cell Stability in Humid Air: Partially Reversible Phase Transitions in the PbI2-CH3NH3I-H2O System. *Adv. Energy Mater.* **2016**, *6*, 1600846.
(37) Wang, S.; Huang, Z.; Wang, X.; Li, Y.; Günther, M.; Valenzuela, S.; Parikh, P.; Cabreros, A.; Xiong, W.; Meng, Y. S. Unveiling the Role of TBP-LiTFSI Complexes in Perovskite Solar Cells. *J. Am. Chem. Soc.* **2018**, *140*, 16720−16730.
(38) Schloemer, T. H.; Christians, J. A.; Luther, J. M.; Sellinger, A. Doping Strategies for Small Molecule Organic Hole-Transport Materials: Impacts on Perovskite Solar Cell Performance and Stability. *Chem. Sci.* **2019**, *10*, 1904−1935.
(39) Xu, P.; Liu, P.; Li, Y.; Xu, B.; Kloo, L.; Sun, L.; Hua, Y. D-A-D-Typed Hole Transport Materials for Efficient Perovskite Solar Cells:

https://dx.doi.org/10.1021/acs.chemmater.0c03772
Chem. Mater. XXXX, XXX, XXX−XXX

Tuning Photovoltaic Properties via the Acceptor Group. *ACS Appl. Mater. Interfaces* **2018**, *10*, 19697−19703.
(40) Chen, Y.; Xu, X.; Cai, N.; Qian, S.; Luo, R.; Huo, Y.; Tsang, S. W. Rational Design of Dopant-Free Coplanar D-π-D Hole-Transporting Materials for High-Performance Perovskite Solar Cells with Fill Factor Exceeding 80%. *Adv. Energy Mater.* **2019**, *9*, 1901268.
(41) Tu, B.; Wang, Y.; Chen, W.; Liu, B.; Feng, X.; Zhu, Y.; Yang, K.; Zhang, Z.; Shi, Y.; Guo, X.; Li, H. F.; Tang, Z.; Djurišić, A. B.; He, Z. Side-Chain Engineering of Donor-Acceptor Conjugated Small Molecules As Dopant-Free Hole-Transport Materials for Efficient Normal Planar Perovskite Solar Cells. *ACS Appl. Mater. Interfaces* **2019**, *11*, 48556−48563.
(42) Franckevičius, M.; Mishra, A.; Kreuzer, F.; Luo, J.; Zakeeruddin, S. M.; Grätzel, M. A Dopant-Free Spirobi[Cyclopenta-[2,1-b:3,4-B′]Dithiophene] Based Hole-Transport Material for Efficient Perovskite Solar Cells. *Mater. Horiz.* **2015**, *2*, 613−618.
(43) Yin, X.; Zhou, J.; Song, Z.; Dong, Z.; Bao, Q.; Shrestha, N.; Bista, S. S.; Ellingson, R. J.; Yan, Y.; Tang, W. Dithieno[3,2-b:2′,3′-d]Pyrrol-Cored Hole Transport Material Enabling Over 21% Efficiency Dopant-Free Perovskite Solar Cells. *Adv. Funct. Mater.* **2019**, *29*, 1904300.
(44) Yang, L.; Cai, F.; Yan, Y.; Li, J.; Liu, D.; Pearson, A. J.; Wang, T. Conjugated Small Molecule for Efficient Hole Transport in High-Performance p-i-n Type Perovskite Solar Cells. *Adv. Funct. Mater.* **2017**, *27*, 1702613.
(45) Wang, Y.; Chen, W.; Wang, L.; Tu, B.; Chen, T.; Liu, B.; Yang, K.; Koh, C. W.; Zhang, X.; Sun, H.; Chen, G.; Feng, X.; Woo, H. Y.; Djurišić, A. B.; He, Z.; Guo, X. Dopant-Free Small-Molecule Hole-Transporting Material for Inverted Perovskite Solar Cells with Efficiency Exceeding 21%. *Adv. Mater.* **2019**, *31*, e1902781.
(46) Cao, Y.; Li, Y.; Morrissey, T.; Lam, B.; Patrick, B. O.; Dvorak, D. J.; Xia, Z.; Kelly, T. L.; Berlinguette, C. P. Dopant-Free Molecular Hole Transport Material That Mediates a 20% Power Conversion Efficiency in a Perovskite Solar Cell. *Energy Environ. Sci.* **2019**, *12*, 3502−3507.
(47) Gangala, S.; Misra, R. Spiro-Linked Organic Small Molecules as Hole-Transport Materials for Perovskite Solar Cells. *J. Mater. Chem. A* **2018**, *6*, 18750−18765.
(48) Bi, D.; Xu, B.; Gao, P.; Sun, L.; Grätzel, M.; Hagfeldt, A. Facile Synthesized Organic Hole Transporting Material for Perovskite Solar Cell with Efficiency of 19.8%. *Nano Energy* **2016**, *23*, 138−144.
(49) Xu, B.; Bi, D.; Hua, Y.; Liu, P.; Cheng, M.; Grätzel, M.; Kloo, L.; Hagfeldt, A.; Sun, L. A Low-Cost Spiro[Fluorene-9,9′-Xanthene]-Based Hole Transport Material for Highly Efficient Solid-State Dye-Sensitized Solar Cells and Perovskite Solar Cells. *Energy Environ. Sci.* **2016**, *9*, 873−877.
(50) Xu, B.; Zhang, J.; Hua, Y.; Liu, P.; Wang, L.; Ruan, C.; Li, Y.; Boschloo, G.; Johansson, E. M. J.; Kloo, L.; Hagfeldt, A.; Jen, A. K. Y.; Sun, L. Tailor-Making Low-Cost Spiro[Fluorene-9,9′-Xanthene]-Based 3D Oligomers for Perovskite Solar Cells. *Chem.* **2017**, *2*, 676−687.
(51) Saliba, M.; Orlandi, S.; Matsui, T.; Aghazada, S.; Cavazzini, M.; Correa-Baena, J. P.; Gao, P.; Scopelliti, R.; Mosconi, E.; Dahmen, K. H.; De Angelis, F.; Abate, A.; Hagfeldt, A.; Pozzi, G.; Graetzel, M.; Nazeeruddin, M. K. A Molecularly Engineered Hole-Transporting Material for Efficient Perovskite Solar Cells. *Nat. Energy* **2016**, *1*, 15017.
(52) Jeon, N. J.; Lee, H. G.; Kim, Y. C.; Seo, J.; Noh, J. H.; Lee, J.; Seok, S., II O-Methoxy Substituents in Spiro-OMeTAD for Efficient Inorganic-Organic Hybrid Perovskite Solar Cells. *J. Am. Chem. Soc.* **2014**, *136*, 7837−7840.
(53) Hu, Z.; Fu, W.; Yan, L.; Miao, J.; Yu, H.; He, Y.; Goto, O.; Meng, H.; Chen, H.; Huang, W. Effects of Heteroatom Substitution in Spiro-Bifluorene Hole Transport Materials. *Chem. Sci.* **2016**, *7*, 5007−5012.
(54) Jeon, N. J.; Na, H.; Jung, E. H.; Yang, T. Y.; Lee, Y. G.; Kim, G.; Shin, H. W.; Il Seok, S.; Lee, J.; Seo, J. A Fluorene-Terminated Hole-Transporting Material for Highly Efficient and Stable Perovskite Solar Cells. *Nat. Energy* **2018**, *3*, 682−689.
(55) Liu, Y.; Hu, Y.; Zhang, X.; Zeng, P.; Li, F.; Wang, B.; Yang, Q.; Liu, M. Inhibited Aggregation of Lithium Salt in Spiro-OMeTAD toward Highly Efficient Perovskite Solar Cells. *Nano Energy* **2020**, *70*, 104483.
(56) Liang, M.; Chen, J. Arylamine Organic Dyes for Dye-Sensitized Solar Cells. *Chem. Soc. Rev.* **2013**, *42*, 3453−3488.
(57) Cinar, M. E.; Ozturk, T. Thienothiophenes, Dithienothiophenes, and Thienoacenes: Syntheses, Oligomers, Polymers, and Properties. *Chem. Rev.* **2015**, *115*, 3036−3140.
(58) Chaitanya, T. K.; Nagarajan, R. Synthesis of Functionalized Ellipticinium and Ellipticine Derivatives via Electrophilic Cyclization. *Org. Biomol. Chem.* **2011**, *9*, 4662−4670.
(59) Rodríguez-Seco, C.; Méndez, M.; Roldán-Carmona, C.; Cabau, L.; Asiri, A. M.; Nazeeruddin, M. K.; Palomares, E. Benzothiadiazole Aryl-Amine Based Materials as Efficient Hole Carriers in Perovskite Solar Cells. *ACS Appl. Mater. Interfaces* **2020**, *12*, 32712−32718.
(60) Zhu, X. D.; Ma, X. J.; Wang, Y. K.; Li, Y.; Gao, C. H.; Wang, Z. K.; Jiang, Z. Q.; Liao, L. S. Hole-Transporting Materials Incorporating Carbazole into Spiro-Core for Highly Efficient Perovskite Solar Cells. *Adv. Funct. Mater.* **2019**, *29*, 1807094.
(61) Pham, H. D.; Wu, Z.; Ono, L. K.; Manzhos, S.; Feron, K.; Motta, N.; Qi, Y.; Sonar, P. Low-Cost Alternative High-Performance Hole-Transport Material for Perovskite Solar Cells and Its Comparative Study with Conventional SPIRO-OMeTAD. *Adv. Electron. Mater.* **2017**, *3*, 1700139.
(62) Shi, D.; Qin, X.; Li, Y.; He, Y.; Zhong, C.; Pan, J.; Dong, H.; Xu, W.; Li, T.; Hu, W.; Brédas, J. L.; Bakr, O. M. Spiro-OMeTAD Single Crystals: Remarkably Enhanced Charge-Carrier Transport via Mesoscale Ordering. *Sci. Adv.* **2016**, *2*, e1501491.
(63) Liu, F.; Wu, F.; Ling, W.; Tu, Z.; Zhang, J.; Wei, Z.; Zhu, L.; Li, Q.; Li, Z. Facile-Effective Hole-Transporting Materials Based on Dibenzo[a, c]Carbazole: The Key Role of Linkage Position to Photovoltaic Performance of Perovskite Solar Cells. *ACS Energy Lett.* **2019**, *4*, 2514−2521.
(64) Azmi, R.; Nam, S. Y.; Sinaga, S.; Akbar, Z. A.; Lee, C. L.; Yoon, S. C.; Jung, I. H.; Jang, S. Y. High-Performance Dopant-Free Conjugated Small Molecule-Based Hole-Transport Materials for Perovskite Solar Cells. *Nano Energy* **2018**, *44*, 191−198.
(65) Rivnay, J.; Mannsfeld, S. C. B.; Miller, C. E.; Salleo, A.; Toney, M. F. Quantitative Determination of Organic Semiconductor Microstructure from the Molecular to Device Scale. *Chem. Rev.* **2012**, *112*, 5488−5519.
(66) Müller-Buschbaum, P. The Active Layer Morphology of Organic Solar Cells Probed with Grazing Incidence Scattering Techniques. *Adv. Mater.* **2014**, *26*, 7692−7709.
(67) Ran, C.; Xu, J.; Gao, W.; Huang, C.; Dou, S. Defects in Metal Triiodide Perovskite Materials towards High-Performance Solar Cells: Origin, Impact, Characterization, and Engineering. *Chem. Soc. Rev.* **2018**, *47*, 4581−4610.
(68) Luo, D.; Su, R.; Zhang, W.; Gong, Q.; Zhu, R. Minimizing Non-Radiative Recombination Losses in Perovskite Solar Cells. *Nat. Rev. Mater.* **2020**, *5*, 44−60.
(69) Wang, S.; Yuan, W.; Meng, Y. S. Spectrum-Dependent Spiro-OMeTAD Oxidization Mechanism in Perovskite Solar Cells. *ACS Appl. Mater. Interfaces* **2015**, *7*, 24791−24798.
(70) Saygili, Y.; Kim, H. S.; Yang, B.; Suo, J.; Muñoz-Garcia, A. B.; Pavone, M.; Hagfeldt, A. Revealing the Mechanism of Doping of Spiro-MeOTAD via Zn Complexation in the Absence of Oxygen and Light. *ACS Energy Lett.* **2020**, *5*, 1271−1277.
(71) Hawash, Z.; Ono, L. K.; Raga, S. R.; Lee, M. V.; Qi, Y. Air-Exposure Induced Dopant Redistribution and Energy Level Shifts in Spin-Coated Spiro-Meotad Films. *Chem. Mater.* **2015**, *27*, 562−569.
(72) Budiawan, W.; Lai, K. W.; Karuppuswamy, P.; Jadhav, T. S.; Lu, Y. A.; Ho, K. C.; Wang, P. C.; Chang, C. C.; Chu, C. W. Asymmetric Benzotrithiophene-Based Hole Transporting Materials Provide High-Efficiency Perovskite Solar Cells. *ACS Appl. Mater. Interfaces* **2020**, DOI: 10.1021/acsami.0c02204.
(73) Kato, Y.; Ono, L. K.; Lee, M. V.; Wang, S.; Raga, S. R.; Qi, Y. Silver Iodide Formation in Methyl Ammonium Lead Iodide

Perovskite Solar Cells with Silver Top Electrodes. *Adv. Mater. Interfaces* **2015**, *2*, 1500195.
(74) Li, J.; Dong, Q.; Li, N.; Wang, L. Direct Evidence of Ion Diffusion for the Silver-Electrode-Induced Thermal Degradation of Inverted Perovskite Solar Cells. *Adv. Energy Mater.* **2017**, *7*, 1602922.

https://dx.doi.org/10.1021/acs.chemmater.0c03772
Chem. Mater. XXXX, XXX, XXX−XXX